Role of crystal-field ground state in the classical spin-liquid behavior of the quasi-one-dimensional spin-chain system Sr_3NiPtO_6

V. K. Anand,[1,2,3,*] D. T. Adroja,[1,4,†] S. Rayaprol,[5] A. D. Hillier,[1] J. Sannigrahi,[1] M. Rotter,[6] M. D. Le,[1] and E. V. Sampathkumaran[5,7]

[1]*ISIS Neutron and Muon Facility, STFC, Rutherford Appleton Laboratory, Chilton, Oxfordshire OX11 0QX, United Kingdom*
[2]*Department of Physics, University of Petroleum and Energy Studies, Dehradun, Uttarakhand 248007, India*
[3]*Department of Mathematics and Physics, University of Stavanger, 4036 Stavanger, Norway*
[4]*Highly Correlated Electron Group, Physics Department, University of Johannesburg, P.O. Box 524, Auckland Park 2006, South Africa*
[5]*UGC-DAE Consortium for Scientific Research, Mumbai Center, R-5 Shed, BARC, Trombay, Mumbai 400085, India*
[6]*McPhase Project, 01159 Dresden, Germany*
[7]*Homi Bhabha Centre for Science Education, Tata Institute of Fundamental Research, V. N. Purav Marg, Mankhurd, Mumbai, 400088 India*

(Received 15 January 2023; revised 21 August 2023; accepted 3 October 2023; published 23 October 2023)

The spin-chain compound Sr_3NiPtO_6 is known to have a nonmagnetic ground state. We investigate the nature of the ground state of Sr_3NiPtO_6 using the magnetic susceptibility $\chi(T)$, heat capacity $C_p(T)$, muon spin relaxation (μSR), and inelastic neutron scattering (INS) measurements. $\chi(T)$ and $C_p(T)$ do not exhibit any pronounced anomaly that can be associated with a phase transition to a magnetically ordered state. Our μSR data confirm the absence of long-range magnetic ordering down to 0.04 K. Furthermore, the muon spin relaxation rate increases below 20 K and exhibits temperature-independent behavior at low temperature, very similar to that observed in a quantum spin-liquid system. The INS data show a large excitation near 8 meV, and the analysis of the INS data reveals a singlet crystal-electric-field (CEF) ground state with a first excited CEF doublet state at $\Delta_{CEF} = 7.7$ meV. The estimated CEF parameters reveal strong planar anisotropy in the calculated $\chi(T)$, consistent with the reported behavior of $\chi(T)$ of single-crystal Sr_3NiPtO_6. We propose that the nonmagnetic singlet ground state and a large Δ_{CEF} (much larger than the exchange interaction $\mathcal{J}_{ex}$) are responsible for the absence of long-range magnetic ordering and can mimic a classical spin-liquid behavior in this quasi-one-dimensional spin-chain system Sr_3NiPtO_6. The classical spin-liquid ground state observed in Sr_3NiPtO_6 is due to the single-ion property, which is different from the quantum spin-liquid ground state observed in geometrically frustrated systems, in which two-ion exchanges play an important role.

DOI: 10.1103/PhysRevB.108.144426

I. INTRODUCTION

Triangular lattice systems are of keen interest because of the novel exotic magnetic states that develop due to the presence of inherent geometric spin frustration on these lattices. Of particular interest are the frustrated quasi-one-dimensional (quasi-1D) spin-chain systems with the general formula $A_3MM'O_6$ (A denotes alkaline metals Sr, Ca, etc., and M and M' denote transition metals), which exhibit a variety of unconventional magnetic properties due to strong spin-orbit coupling (SOC) and reduced dimensionality [1–34]. These spin-chain materials crystallize in the K_4CdCl_6-type hexagonal structure (space group $R\bar{3}c$) consisting of 1D spin chains aligned along the c axis which are formed by alternating a face-sharing MO_6 trigonal prism and $M'O_6$ octahedra and are arranged on a triangular lattice in the ab plane [1–3]. As the presence of two different transition metal ions in these materials may provide multiple exchange paths, these materials are quite interesting from both experimental and theoretical view points.

Ca-based spin-chain compounds have been rigorously investigated [5–14]; however, detailed investigations of their Sr-based counterparts are still lacking. Sr_3MgMO_6 (M = Pt, Ir, Rh), Sr_3ZnRhO_6, and Sr_3MIrO_6 (M = Co, Cu, Ni, and Zn) are some of the known Sr-based spin-chain compounds. [15–34]. Recently, some of us performed microscopic investigations of Sr_3ZnRhO_6 [18], Sr_3ZnIrO_6 [23], and Sr_3NiIrO_6 [24] using neutron scattering and muon spin relaxation techniques. Sr_3MIrO_6 (M = Co, Cu, Ni, and Zn) exhibits diverse physical properties due to the competing SOC, magnetic exchange, and crystal-field interactions as a result of the coexistence of 3d and 5d metals [19–34]. Further, in these Sr spin chains, in addition to the presence of SOC, a strong intrachain exchange coupling may also exist, resulting in an anisotropic exchange interaction, as seen in Sr_3CuIrO_6 [21]. Strong SOC may open a gap in the electronic spectrum, driving the system to an insulating state, the so-called spin-orbit-driven Mott insulator state.

The spin-chain systems having both M and M' moment-carrying transition metals present very interesting magnetic behavior, as is the case for Sr_3NiIrO_6, which hosts alternating

*vivekkranand@gmail.com
†devashibhai.adroja@stfc.ac.uk

chains of spin-1/2 (Ir^{4+} occupying the octahedral site) and spin-1 (Ni^{2+} occupying the trigonal prism site) ions along the c axis [24–34]. The magnetic state of Sr_3NiIrO_6 is characterized by a magnetic phase transition below 75 K and a spin-freezing-type anomaly below 17 K in the magnetization and a large single-ion anisotropy [24–34]. A neutron diffraction study found magnetic peaks below 75 K, and the magnetic structure is described by propagation vector $\mathbf{k} = (0, 0, 1)$ [29]. Based on the symmetry analysis an amplitude-modulated antiferromagnetic arrangement of ferrimagnetic chains of Ir^{4+} and Ni^{2+} is suggested for the magnetic phase between 2 and 75 K [29]. Despite the presence of a clear anomaly in the magnetization at 17 K, the neutron diffraction study did not see any change in the magnetic structure going through the 17 K transition in Sr_3NiIrO_6. An inelastic neutron scattering (INS) study revealed a large energy gap (∼30 meV) in magnetic excitations with a quasi-1D nature for the magnetic interaction [24]. Infrared and optical spectroscopies revealed spin-charge-lattice entanglement and the presence of vibronic coupling in Sr_3NiIrO_6 [31].

Sr_3NiPtO_6, which hosts magnetic Ni^{2+} ($3d^8$, $S = 1$) and nonmagnetic Pt^{4+} ($5d^6$, $S = 0$), is another interesting compound which is suggested to have a spin-liquid-like ground state [2–4,32–37]. No evidence of long-range magnetic ordering has been found for temperatures down to 1.8 K, although an anomaly associated with low-dimensional short-range magnetic ordering is seen in magnetic susceptibility around 25–30 K [2,32]. Magnetic measurements on single-crystal Sr_3NiPtO_6 revealed a large easy-plane magnetic anisotropy which is described by a model of noninteracting Ni^{2+} with a large magnetocrystalline anisotropy parameter $\mathcal{D} \sim 7.5-9.3$ meV [3,34], indicating a large-$\mathcal{D}$ magnetic phase in this compound. A large-$\mathcal{D}$ magnetic phase is realized in quantum spin-chain systems when the condition $\mathcal{D}/\mathcal{J}_{ex} > 1$ is fulfilled, where $\mathcal{J}_{ex}$ represents the magnetic exchange interaction [34,38,39]. Theoretical attempts have been made to explain the observed magnetic behavior of this compound [33,35,36]. While density functional theory (DFT) calculations correctly predicted an easy-plane anisotropy, they underestimated the magnitude [36], whereas a wave-function-based complete active space perturbation theory (CASPT2) approach yielded more accurate predictions [36].

Despite several experimental and theoretical works on the subject, the nature of the magnetic ground state in Sr_3NiPtO_6 is still not clear and invites further investigation. The present work aims to exemplify the nature of the magnetic ground state of Sr_3NiPtO_6 through microscopic investigations. We probed the magnetic properties using muon spin relaxation (μSR), which found the absence of long-range magnetic ordering down to 0.04 K. The inelastic neutron scattering measurements enable us to determine the crystal-electric-field (CEF) level scheme. The magnetization M as a function of temperature T and magnetic field H, and heat capacity $C_p(T)$ data are also presented here to characterize the sample quality via a comparison with the reported results. Our remaining discussion is divided into three sections. We present experimental details in Sec. II. The results of magnetization, heat capacity, μSR, and INS measurements are presented in Sec. III. Finally, a summary of the results and conclusions is given in Sec. IV.

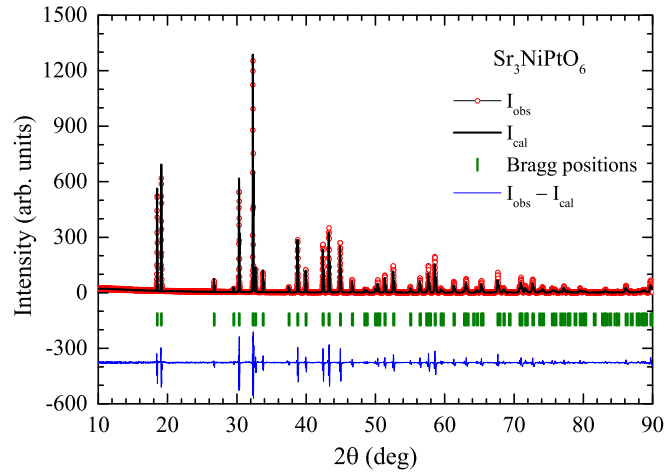

FIG. 1. X-ray powder diffraction pattern of Sr_3NiPtO_6 recorded at room temperature. The solid line through the experimental points is the Le Bail profile fit for K_4CdCl_6-type hexagonal structure (space group $R\bar{3}c$). The short vertical bars mark the Bragg peak positions. The lowermost curve represents the difference between the observed and calculated intensities.

Our results indicate that Sr_3NiPtO_6 indeed presents all the properties expected for a classical spin-liquid phase rather than a quantum spin-liquid behavior.

II. EXPERIMENTAL DETAILS

A polycrystalline sample of Sr_3NiPtO_6 was prepared following the solid-state reaction route in air starting with the high-purity materials $SrCO_3$ (99.99%), NiO (99.99%), and PtO_2 (99.99%) in powder form. The thoroughly mixed powders of the constituent components in a stoichiometric ratio were calcined at 800 °C for 24 h. After initial calcination, the powder was pressed into pelletized form and sintered at 1000 °C for 9 days with three intermediate grindings as described in Ref. [32].

The quality of the sample was examined by room temperature x-ray diffraction (XRD), performed on the powdered sample of Sr_3NiPtO_6, which is shown in Fig. 1. The Le Bail profile fit for the reported hexagonal structure (space group $R\bar{3}c$) of Sr_3NiPtO_6 [2,3] is shown in Fig. 1. All the observed XRD peaks are consonant with the Bragg peaks expected in space group $R\bar{3}c$ and are well captured by the Le Bail profile fit. The single-phase nature of the synthesized sample is evident from Fig. 1. The lattice parameters a=9.5888(1) Å and c = 11.2003(2) Å obtained from XRD are found to be in very good agreement with the reported values [2,3].

The magnetic susceptibility $\chi(T)$, isothermal magnetization $M(H)$, and heat capacity $C_p(T)$ measurements were carried out using a Quantum Design superconducting quantum interference device vibrating-sample magnetometer and physical properties measurement system. The μSR experiments were carried out using the MuSR spectrometer at the ISIS Neutron and Muon Facility, United Kingdom. μSR measurements were done in zero magnetic field. The powdered sample was mounted on an Ag plate using GE varnish. Temperatures down to 0.04 K were achieved by using a dilution stick in a ^{4}He cryostat. For temperatures between 0.04 and 4 K the data

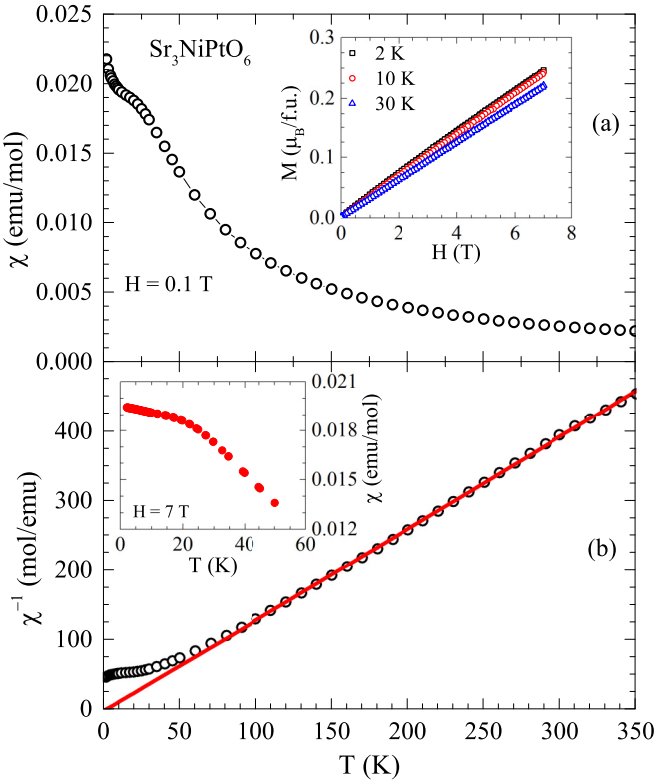

FIG. 2. (a) Temperature T variation of the magnetic susceptibility χ of Sr_3NiPtO_6 for $1.8 \leqslant T \leqslant 350$ K measured in magnetic field $H = 0.1$ T. The inset shows the magnetization $M(H)$ isotherms at indicated temperatures. (b) Inverse susceptibility plot $\chi^{-1}(T)$. The solid line is the fit to modified Curie-Weiss law. The inset shows the low-T $\chi(T)$ measured in $H = 7$ T.

were collected under vacuum, and for 4 to 50 K He-exchange gas was added in the sample space [40]. Spin-polarized positive muons (μ^+, mean lifetime of 2.2 μs, momentum of 28 MeV/c, and $\gamma_\mu/2\pi = 135.5\,\mathrm{MHz\,T^{-1}}$) were implanted into the polycrystalline sample. The average spin polarization of the muons stopped within the sample is proportional to the decay positron asymmetry function $A(t)$ [41,42].

The inelastic neutron scattering measurements were carried out on the high energy transfer (HET) time-of-flight spectrometer at ISIS Neutron and Muon Facility with incident neutron energies E_i of 15, 50, and 900 meV at several temperatures from 4.5 to 300 K. The powdered sample (total mass of 8 g) was mounted in a thin Al-foil envelope, which was cooled down to 4.5 K using a closed-cycle refrigerator (CCR) in the presence of He-exchange gas.

III. RESULTS

A. Magnetic susceptibility and heat capacity

The results of dc $\chi(T)$ and $M(H)$ measurements for Sr_3NiPtO_6 are shown in Fig. 2. We do not see any sharp anomaly associated with long-range magnetic ordering in $\chi(T)$ down to 1.8 K. The weak anomaly attributable to short-range ordering, as reported for the polycrystalline samples [2,32], is present in our $\chi(T)$ data. It is seen from Fig. 2(a) that at an applied magnetic field of 0.1 T χ increases monotonically with decreasing temperature. At T below ~30 K, a tendency to flatten is observed, as often found in low-dimensional systems. Additionally, an upturn is also present in our data below 10 K, known as a Curie tail, which could be due to the presence of paramagnetic impurities. $\chi(T)$ follows the modified Curie-Weiss law, $\chi(T) = \chi_0 + C/(T - \theta_p)$, at temperatures above 100 K. Our fit of the inverse susceptibility to the modified Curie-Weiss law in the range $100 \leqslant T \leqslant 350$ K [see Fig. 2(b)] yielded $\chi_0 = 4.3(6) \times 10^{-5}$ emu/mol, an effective paramagnetic moment $\mu_{\mathrm{eff}} = 2.48(7)\mu_{\mathrm{B}}$, and a small, but positive, Weiss temperature $\theta_p = 2.6(1.0)$ K. The value of μ_{eff} obtained from our data is close to that of the spin-only value for Ni^{2+} (d^8), which is 2.83 μ_B. Since Pt^{4+} (d^6) is in the low-spin ($S = 0$) state and is believed not to possess a magnetic moment, it is quite natural to achieve a μ_{eff} close to the spin-only value of Ni^{2+}. A small interchain interaction with a value of 0.10 meV was reported from the DFT calculation, which turned out to be ferromagnetic [33] and can be correlated with the small, positive θ_p observed from our data. The values of θ_{p} and μ_{eff} obtained above differ from the previously reported values [2,32]. However, if we fit the $\chi(T)$ data by the Curie-Weiss law we get a negative θ_{p} [$= -8.5(6)$ K], and the value of μ_{eff} comes out to be $3.25(5)\mu_{\mathrm{B}}$, consistent with the literature values [2,32].

Further, we measured $\chi(T)$ in the presence of a higher applied magnetic field of 7 T, and we see that the Curie tail becomes saturated and almost temperature independent at low T [see the inset in Fig. 2(b)]. This Van Vleck paramagnetism (the constant susceptibility) at low temperature could be related to a singlet CEF ground state. The isothermal $M(H)$ at 2, 10, and 30 K are shown in the inset in Fig. 2(a), and they are practically linear at all three temperatures for H up to 7 T.

Figure 3(a) displays the T variation of the heat capacity of Sr_3NiPtO_6 between 1.8 and 60 K. For comparison, the $C_{\mathrm{p}}(T)$ data of the nonmagnetic reference compound Sr_3ZnPtO_6 (from Ref. [34]) are also presented. The absence of an anomaly in $C_{\mathrm{p}}(T)$ data down to the lowest measured temperature clearly indicates the absence of long-range ordering. We see that the heat capacity is extremely small at temperatures below 5 K [see the inset in Fig. 3(a)]. Such a feature of heat capacity is an indication of the presence of a gap in the spin excitation spectra in Sr_3NiPtO_6.

The $C_{\mathrm{p}}(T)$ data of Sr_3ZnPtO_6 [34] were used to estimate the phonon contribution to the heat capacity of Sr_3NiPtO_6. However, since the formula masses and unit cell volumes of Sr_3NiPtO_6 and Sr_3ZnPtO_6 are different, the measured T of Sr_3ZnPtO_6 was scaled according to [43,44]

$$T^* = T\left(\frac{M_{\mathrm{Sr_3NiPtO_6}}}{M_{\mathrm{Sr_3NiZnO_6}}}\right)^{1/2}\left(\frac{V_{\mathrm{Sr_3NiPtO_6}}}{V_{\mathrm{Sr_3NiZnO_6}}}\right)^{1/3}, \qquad (1)$$

where M is the formula mass and V is the volume per formula unit. The scaled $C_{\mathrm{p}}(T^*)$ of Sr_3ZnPtO_6 was then taken as the lattice contribution to separate out the magnetic contribution to the heat capacity $C_{\mathrm{mag}}(T)$ of Sr_3NiPtO_6. $C_{\mathrm{mag}}(T)$ estimated this way is presented in Fig. 3(b) along with the literature data for $C_{\mathrm{mag}}(T)$ from Ref. [34] and is compared to $C_{\mathrm{mag}}(T)$ obtained using the crystal-electric-field parameters based on the analysis of inelastic neutron scattering data (see Sec. III C). As can be seen from Fig. 3(b) our $C_{\mathrm{mag}}(T)$ agree very well with

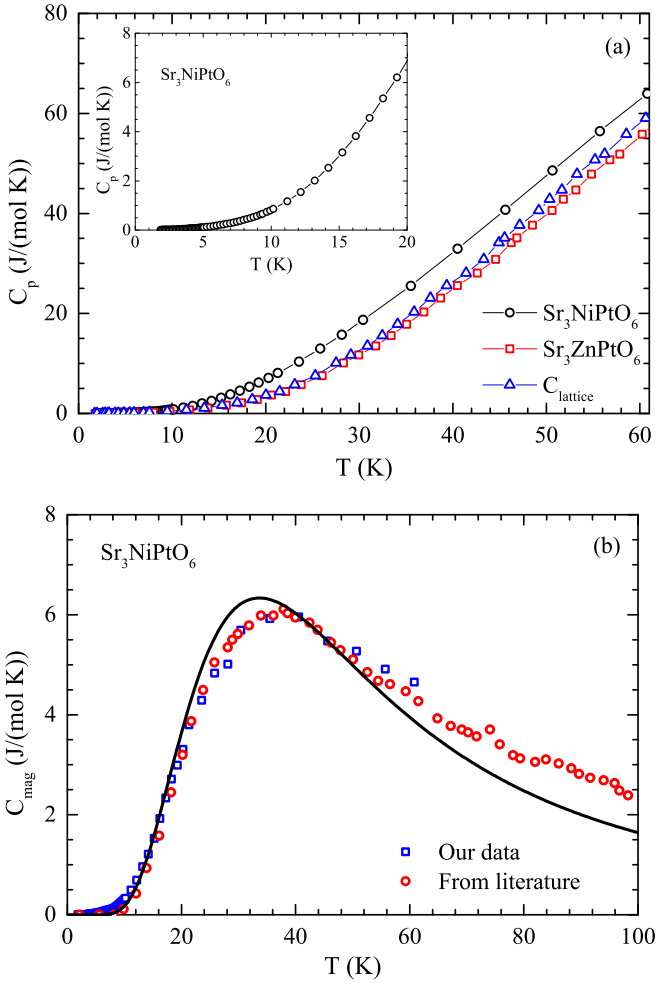

FIG. 3. (a) Temperature T variation of the heat capacity C_p of Sr_3NiPtO_6 for $1.8 \leqslant T \leqslant 60$ K measured in zero field together with $C_p(T)$ of the nonmagnetic reference compound Sr_3ZnPtO_6 from Ref. [34]. The lattice contribution $C_{lattice}(T)$ was obtained by scaling $C_p(T)$ of Sr_3ZnPtO_6 according to Eq. (1) as discussed in text. The inset is an expanded plot of $C_p(T)$ of Sr_3NiPtO_6 for $T < 20$ K. (b) Magnetic heat capacity $C_{mag}(T)$ for Sr_3NiPtO_6 along with the $C_{mag}(T)$ data from Ref. [34] for comparison. The solid curve represents $C_{mag}(T)$ estimated using the CEF parameters obtained from the analysis of the inelastic neutron scattering data.

the literature data and present a broad Schottky-type anomaly which is well captured by the CEF level scheme.

B. Muon spin relaxation

The zero-field (ZF) asymmetry μSR spectra for Sr_3NiPtO_6 are shown in Fig. 4 for four representative temperatures: 0.04, 3, 10, and 30 K. As can be seen from Fig. 4, down to 0.04 K ZF signals do not show any clear sign of oscillations within the analyzed time window up to 20 μs. The observation that at both high and low temperatures (down to 0.04 K) μSR spectra relax in a similar way with nearly the same values of the initial asymmetry excludes the presence of long-range magnetic ordering in Sr_3NiPtO_6. The zero-field spectra also lack the recovery of the one third of the polarization which signifies the absence of static random field, which gives a

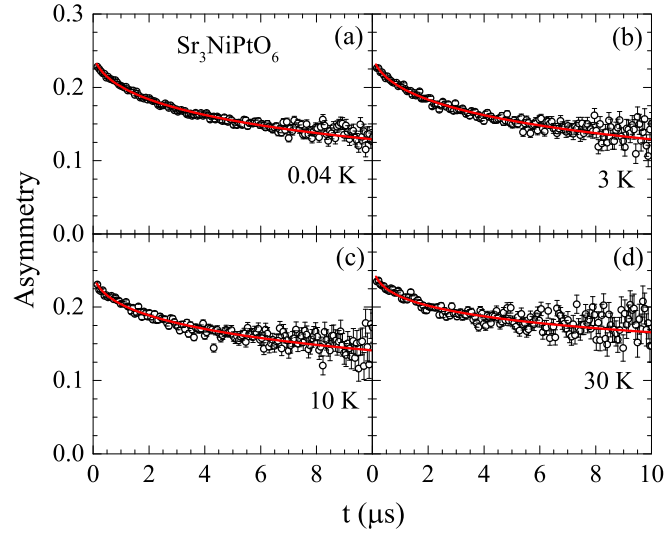

FIG. 4. Zero-field μSR asymmetry vs time t spectra of Sr_3NiPtO_6 at indicated temperatures. The red solid curves are the fits to the μSR data using Eq. (2).

Kubo-Toyabe-type relaxation. We thus see that the μSR spectra do not show any evidence of a magnetic phase transition down to 0.04 K.

The form of the relaxation depends on the distribution and time dependence of the local magnetic fields around the muon implanted sites. Our ZF data are well fitted by a stretched exponential function,

$$A = A_0 \exp[-(\lambda t)^{\beta}] + A_{BG}, \tag{2}$$

where A_0 is the initial asymmetry, λ is the μ^+ spin relaxation rate, β is an exponent, and A_{BG} is the background contribution to muon asymmetry. We choose the constant background $A_{BG} \approx 0.04$ representing muons that missed the sample and stopped on the Ag sample holder. The fitting parameters obtained from the fits of ZF-μSR spectra by Eq. (2) are presented in Fig. 5. Fits are shown by red solid curves in Fig. 4. The asymmetry A_0 shows a weak temperature dependence, decreases from 0.26 (at 50 K) to 0.21 (at 4 K), and remains unchanged between 0.04 and 4 K. The relaxation rate λ shows a strong temperature dependence, increases rapidly below 20 K, and eventually saturates at $T \leqslant 4$ K, as can be seen more clearly from the logarithmic-scale plot in Fig. 5(d). The exponent β is also seen to increase with decreasing T [Fig. 5(c)]. The fact that the μSR data could not be described by the classical exponential function ($\beta = 1$) reflects that our system is not a simple paramagnetic system. The stretched exponential fit yields β values much lower than 1, which reveals that there is a distribution of relaxation times in Sr_3NiPtO_6 as expected when different spins do fluctuate on different timescales. For a spin-glass system β is expected to reach a value of 1/3 when the system approaches the spin-glass freezing temperature. As can be seen from Fig. 5(c), for the present compound β reaches 1/2, which is not consistent with the spin-glass freezing in this compound. However, all these results are consistent with a spin-liquid-like behavior in Sr_3NiPtO_6. Further, the observed temperature dependence of λ (T-independent behavior of λ at low T) is very similar to that observed in the frustrated

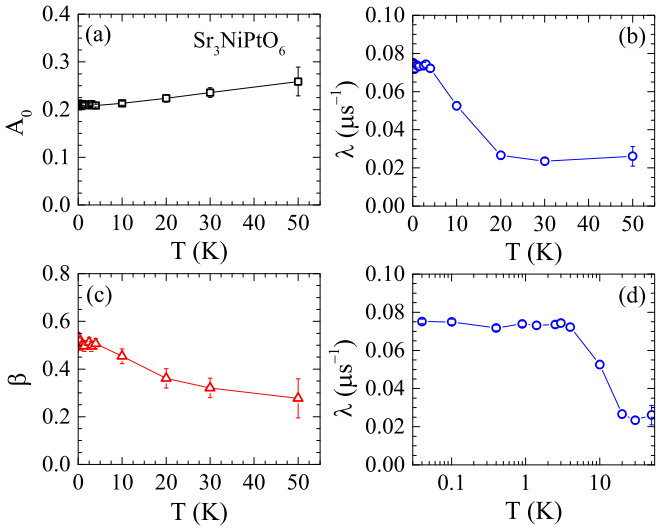

FIG. 5. Temperature T dependence of the fit parameters: (a) muon initial asymmetry A_0, (b) relaxation rate λ, and (c) exponent β obtained from the fitting of the zero-field μSR spectra by Eq. (2). (d) The T dependence of λ plotted on a semilogarithmic scale.

magnet $SrCr_8Ga_4O_{19}$ [45] and in the quantum spin-liquid materials $NaYbS_2$ [46] and $YbMgGaO_4$ [47]. This signifies a fluctuating spin dynamics consistent with the proposed spin-liquid-like behavior in Sr_3NiPtO_6. We would like to point out that the quantum spin-liquid behavior (no magnetic ordering down to 0 K) arises due to magnetic frustration (two or more ions exchange interactions), while the classical spin liquid we observe in Sr_3NiPtO_6 is due to a single-ion effect arising from the nonmagnetic ground state.

C. Inelastic neutron scattering

Figures 6(a) and 6(b) show temperature-dependent two-dimensional (2D) color-coded intensity maps of energy E transfer vs momentum $|Q|$ transfer for Sr_3NiPtO_6 measured with incident neutrons of energy $E_i = 15$ meV. The data are from the low-angle scattering banks of the HET spectrometer between 3.5° and 30°. At 4.5 K we see very strong excitation near 8 meV. The intensity of this excitation was absent in the high-angle bank at 110° and 135°, which reflects the magnetic origin of this excitation. Further, with increasing temperature the intensity of this excitation decreases, and the presence of the excitation can clearly be seen even at 300 K (data not shown). Q-integrated 1D energy cuts of INS responses for inelastic scattering intensity $S(Q, \omega)$ versus E are plotted in Figs. 6(c) and 6(d) for representative temperatures of 4.5 and 100 K. The decrease in the intensity of the excitation with increasing temperature can be seen very clearly in the 1D cuts. Further, we see that with increasing temperature the inelastic peak on the neutron energy gain side becomes visible due to the thermal population factor of the 8 meV excitation. It should be noted that the temperature-independent shoulder on the elastic line near 1 meV energy transfer is the background from the CCR due to multiple scattering.

Figure 7(a) shows a color-coded 2D intensity map of the inelastic neutron scattering response for a measurement with a higher incident energy $E_i = 50$ meV at 50 K in order to cover the larger range of E-Q space to investigate the Q dependence of the intensity of the 8 meV excitation. In Fig. 7(b) we plot the Q dependence of the energy-integrated intensity (integrated between 6.5 and 9.5 meV) of the 8 meV excitation. It is evident that the intensity of this peak decreases with increasing Q, which indicates the magnetic nature of this excitation. To further confirm that the intensity of this peak follows the Ni^{2+} squared magnetic form factor $F^2(Q)$ [48], we also plot the squared magnetic form factor, the solid curve in Fig. 7(b) which passes through the experimental data. This confirms that the 8 meV peak originates from the Ni^{2+} ion. We also performed high energy $E = 900$ meV measurements at 5 and 300 K, and we did not find any clear signature of the presence of any additional magnetic excitation in this energy range (see Fig. 10 in the Appendix).

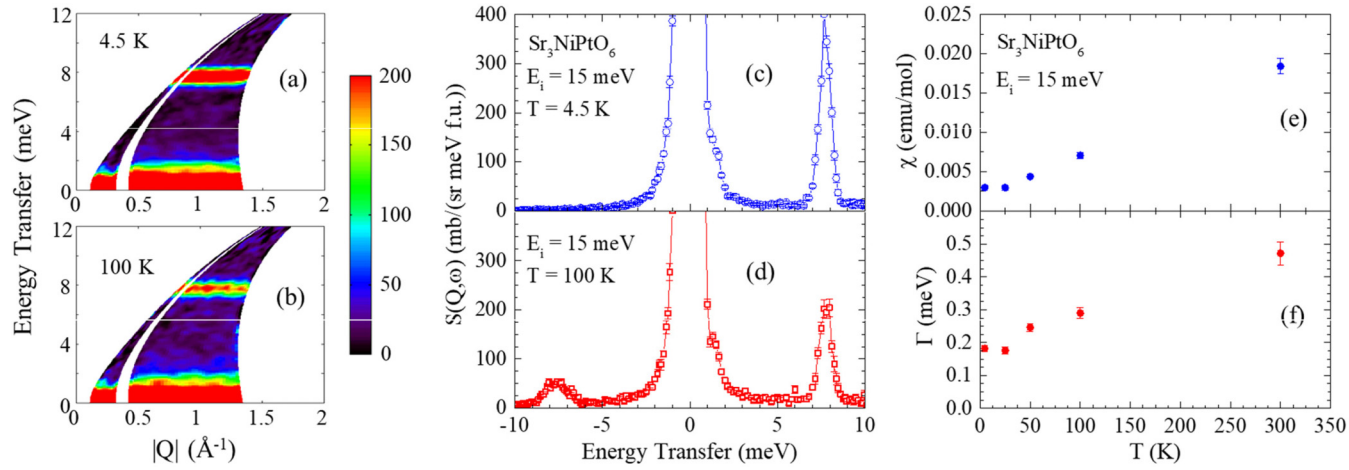

FIG. 6. Inelastic neutron scattering response, shown as a color-coded contour map of the intensity, of the energy E transfer vs momentum $|Q|$ transfer for Sr_3NiPtO_6 measured at representative temperatures of (a) 4.5 K and (b) 100 K, using neutrons with incident energy $E_i =$ 15 meV. Corresponding Q-integrated (between 0 and 2 Å^{-1}) 1D energy cuts of INS responses for inelastic scattering intensity $S(Q, \omega)$ versus E at (c) 4.5 K and (d) 100 K. Temperature T dependence of the fit parameters, that is, (e) susceptibility χ (amplitude of the Lorentzian) vs T and (f) linewidth Γ vs T, obtained from fitting the 1D energy cuts to a Lorentzian function convoluted with the instrument resolution.

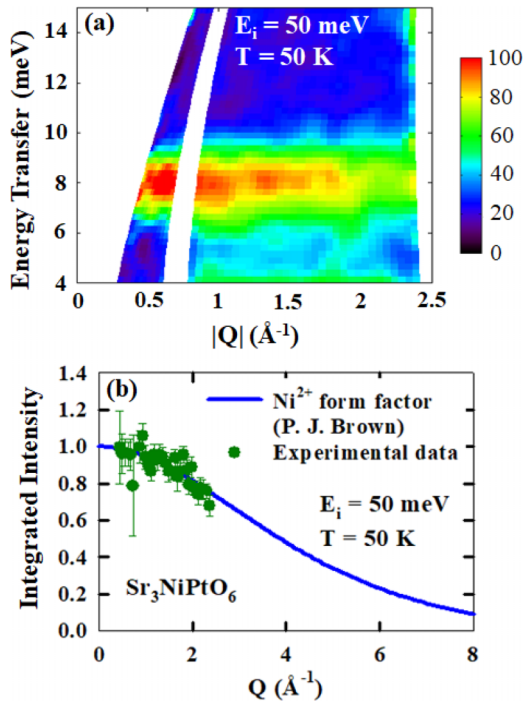

FIG. 7. (a) Color-coded INS intensity of Sr_3NiPtO_6 measured at 50 K with neutrons of incident energy $E_i = 50$ meV. (b) Energy-integrated, Q-dependent intensity between 6.5 and 9.5 meV (solid symbols) obtained from the INS response in (a). The solid curve in (b) shows the squared magnetic form factor $F^2(Q)$ of Ni^{2+} from Brown [48] scaled to 1 at $Q = 0$.

In order to gain further information about the nature of the 8 meV excitation, we fit the $S(Q, \omega)$ versus E data using a Lorentzian function convoluted with the instrument resolution function, which provides information about the static susceptibility, position, and linewidth of this peak. The static susceptibility (amplitude of the Lorentzian) and linewidth Γ (HWHM) obtained from the fits of $S(Q, \omega)$ are plotted in Figs. 6(e) and 6(f). Further, to check the temperature dependence of the linewidth Γ we also plotted Γ vs $T^{1/2}$ as well as Γ vs T^2 (not shown), and we found that, overall, the T dependence of Γ between 4.5 and 300 K is described best by a linear behavior.

We estimate the effective paramagnetic moment from the 8 meV peak by using the moment sum rule, according to which

$$\int \frac{S(Q,\omega)}{F^2(Q)} d\omega = A\mu_{\text{eff}}^2, \tag{3}$$

where the constant $A = (2/3)(r_0/2)^2$, with $r_0 = g_n r_e/2$, where r_e is the classical electron radius and g_n is the neutron g factor. With the values of g_n and r_e, $A = 48.43\,\text{mb/(sr}\,\mu_B^2)$. The integrated intensity for the 8 meV peak is found to be 350(7) mb/sr; accordingly, we obtain $\mu_{\text{eff}} = 2.68(4)\mu_B$ at 4.5 K, which is in good agreement with the value of $\mu_{\text{eff}} = 2.5\mu_B$ obtained from the analysis of $\chi(T)$ and with the theoretically expected value of $2.83\mu_B$ for Ni^{2+} ions. As the deduced μ_{eff} is close to the full value expected for Ni^{2+}, it implies that the whole spectral weight has been accounted for and no other excitation should be visible.

TABLE I. Crystal-electric-field level scheme obtained from the analysis of the inelastic neutron scattering data. The 21-fold degenerate ground state multiplet of Ni^{2+} ($L = 3$ and $S = 1$) splits into a combination of 7 singlets and 7 doublets. Splitting energies are relative to the ground state energy (set to zero).

Level	Splitting energy (meV)	Splitting energy (K)
Singlet	0	0
Doublet	7.7	89.4
Doublet	134.9	1565.6
Doublet	192.5	2233.8
Singlet	202.8	2352. 9
Singlet	231.5	2686.3
Doublet	280.3	3253.2
Singlet	300.6	3488.0
Doublet	345.6	4011.0
Singlet	359.6	4172.9
Singlet	451.7	5241.3
Singlet	463.6	5380.2
Doublet	552.4	6409.9
Doublet	605.0	7020.5

We now present an analysis of CEF excitations based on the CEF model. The crystal-field Hamiltonian (in Wybourne normalization) relevant for the point symmetry D_3 of Ni^{2+} ions in Sr_3NiPtO_6 is given by

$$H_{\text{CEF}} = L_{20}\hat{T}_{20} + L_{40}\hat{T}_{40} + L_{43}\hat{T}_{43}, \tag{4}$$

where L_{lm} are crystal-field parameters with the same normalization as the Wybourne parameters but are real numbers and $\hat{T}_{lm}$ are tensor operators defined in the MCPHASE program [49], which are the Hermitian combinations of the Wybourne tensor operators $\hat{C}_{lm}$. The relation between CEF parameters L_{lm} used here and conventional Stevens CEF parameters B_n^m [50] is given by $B_n^m = \lambda_{lm} L_{lm} \langle L||\theta_l||L\rangle$, where the values of normalization constants λ_{lm} are given in [49] and $\langle L||\theta_l||L\rangle$ are the orbital Stevens operator equivalent factors (θ_l for $l = 0$, 2, 4, 6) given for Ni^{2+} by Abragam and Bleaney [51].

We used the MCPHASE program [49] to analyze our inelastic data and calculate the physical properties. First, we used the point-charge model for an initial estimation of the crystal-field parameters L_{lm}. The estimated L_{lm} CEF parameters from the point charge model gave an INS excitation near 15 meV, compared to the observed 8 meV excitation. Then we kept the values of L_{40} and L_{43} fixed from the point charge estimation and manually varied the value of L_{20} to get good agreement between the observed and calculated CEF excitations. We found that when we divide the point charge value of L_{20} by a factor of 3.5, we get very good agreement between the data and calculation. The ground state is a singlet with the first excited doublet at 7.7 meV (two singlets with the same energy), and the overall splitting energy is found to be ≈ 605 meV. The L_{lm} parameters obtained are $L_{20} = 80.26$ meV, $L_{40} = -609.96$ meV, and $L_{43} = -180.15$ meV (corresponding value of Stevens parameters are $B_2^0 = 0.764$ meV, $B_4^0 = -0.484$ meV, and $B_4^3 = -3.383$ meV). All 21 energy levels of Ni^{2+} ($L = 3$ and $S = 1$) obtained from the analysis of the INS data are listed in Table I. The ground state

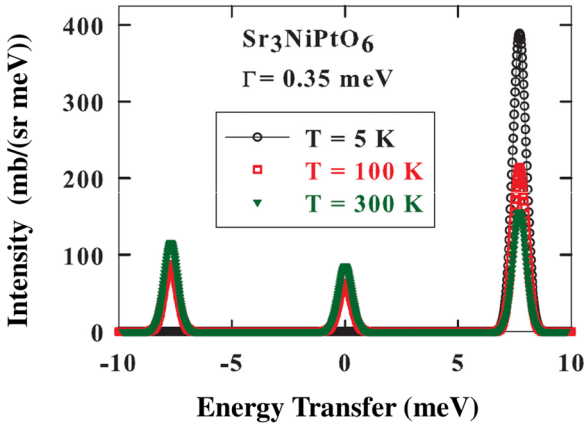

FIG. 8. Calculated crystal-electric-field excitations of Ni^{2+} at 5, 100, and 300 K for Sr_3NiPtO_6 calculated using the MCPHASE program for the L_{lm} parameters obtained from the analysis of the inelastic neutron scattering data. The excitations are calculated at $Q = 0$.

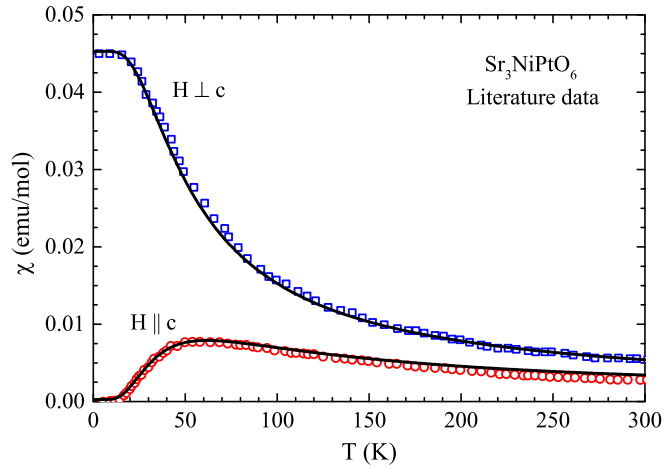

FIG. 9. Calculated single-crystal magnetic susceptibility $\chi(T)$ (solid lines) and the experimental data from Ref. [34] (symbols) for comparison. $\chi(T)$ was calculated using the CEF parameters obtained from the analysis of the inelastic neutron scattering data.

wave function is found to be

$$\Psi_0 = -0.885|^3F_4, m_J = 0\rangle + 0.252|^3F_2, m_J = 0\rangle + 0.198|^3F_3, m_J = 3\rangle + 0.198|^3F_3, m_J = -3\rangle,$$

and the wave function for the first excited state is

$$\Psi_1 = \pm 0.706|^3F_4, m_J = \mp 1\rangle - 0.530|^3F_4, m_J = \mp 4\rangle - 0.417|^3F_3, m_J = \mp 1\rangle \pm 0.129|^3F_2, m_J = \mp 1\rangle.$$

The calculated CEF excitations for Ni^{2+} using MCPHASE for the above obtained L_{lm} parameters are shown in Fig. 8 for temperatures of 5, 100, and 300 K. We can see that the 8 meV excitation is well reproduced by the CEF parameters. It should be noted that only one strong CEF excitation near 8 meV is seen in the calculation, which is in agreement with the experimental observation. Next, we use the CEF parameters to calculate the single-crystal magnetic susceptibility $\chi(T)$ for $H \parallel c$ and $H \perp c$, which is presented in Fig. 9. Our calculated $\chi(T)$ data clearly show strong anisotropy and are in qualitative agreement with the experimental $\chi(T)$ of single-crystal Sr_3NiPtO_6 reported in Ref. [34], which are also presented in Fig. 9 for comparison. We also calculated the magnetic heat capacity $C_{mag}(T)$ using the CEF parameters, which is presented in Fig. 3(b) along with our experimental $C_{mag}(T)$ data and the literature data from Ref. [34]. Our CEF model heat capacity reproduces the experimental $C_{mag}(T)$ data for Sr_3NiPtO_6 very well.

The occurrence of long-range magnetic ordering in a singlet ground state system depends on the relative strength of the exchange interaction $\mathcal{J}_{ex}$ and the CEF splitting energy Δ_{CEF} (between the ground state and the first excited state). An induced moment ordering is possible, provided the critical value of $\mathcal{J}_{ex}$ fulfills the condition $4\mathcal{J}_{ex}\alpha^2/\Delta_{CEF} \geqslant 1$, where α is the matrix element of angular momentum between the CEF ground state and CEF excited state [52–54]. The exchange energy $\mathcal{J}_{ex}$ can be estimated from the value of θ_p as [55,56]

$$\theta_p = -\frac{\mathcal{J}_{ex}\, S(S+1)}{3k_B}, \tag{5}$$

where $\mathcal{J}_{ex} = \sum_j \mathcal{J}_{ij}$ and k_B is Boltzmann's constant. For Sr_3NiPtO_6, the analysis of $\chi(T)$ yielded $\theta_p = +2.6$ K; accordingly, for Ni^{2+} ($3d^8$, $S = 1$), $\mathcal{J}_{ex} = -0.336$ meV. This value of $|\mathcal{J}_{ex}| = 0.336$ meV (≈3.9 K) is much smaller than the CEF splitting energy $\Delta_{CEF} = 7.7$ meV (≈89 K) between the ground state singlet and the first excited doublet and does not fulfill the condition for induced moment ordering. It appears that it is the presence of the nonmagnetic CEF-split singlet ground state and $\Delta_{CEF} \gg \mathcal{J}_{ex}$ which together create a very unfavorable condition for the development of long-range magnetic ordering, and in the absence of long-range ordering a classical spin-liquid behavior (originating from the single-ion exchange effect) is observed in Sr_3NiPtO_6.

IV. CONCLUSIONS

We investigated the electronic and magnetic ground state of Sr_3NiPtO_6 using $\chi(T)$, $M(H)$, $C_p(T)$, muon spin relaxation, and inelastic neutron scattering measurements in order to understand the proposed spin-liquid behavior in this quasi-one-dimensional spin-chain system. $\chi(T)$ and $C_p(T)$ do not show any sign of long-range magnetic ordering down to 2 K. The absence of long-range ordering down to 0.04 K was further confirmed by the μSR data, consistent with the spin-liquid behavior. The μSR data are well described by a stretched exponential relaxation function. Our analysis of zero-field μSR spectra revealed a weak relaxation above 20 K, and below 20 K there is an increase in the relaxation rate with a nearly temperature independent saturating behavior between 4 and 0.04 K. The μSR data reflect a spin-liquid-like spin dynamics in Sr_3NiPtO_6.

The inelastic neutron scattering showed a strong excitation near 8 meV. The analysis of INS data revealed a singlet CEF ground state with the first excited doublet state at $\Delta_{CEF} = 7.7$ meV. The magnetic susceptibility calculated using the CEF parameters obtained from the analysis of INS data revealed a strong planar anisotropy and is qualitatively in very good agreement with the reported single-crystal sus-

ceptibility data. The absence of long-range magnetic ordering, and hence the spin-liquid-like behavior in Sr_3NiPtO_6, can be attributed to the presence of a nonmagnetic CEF singlet ground state and a large CEF splitting between the ground state and the first excited doublet, $\Delta_{CEF} \gg \mathcal{J}_{ex}$. Further, it is the single-ion exchange property of Ni^{2+} which is responsible for the spin-liquid-like behavior in Sr_3NiPtO_6. This mechanism is different from the two-ion exchange-driven quantum spin-liquid state observed in geometrically frustrated systems [57–59], and hence, we call it classical spin-liquid behavior in Sr_3NiPtO_6. Our results will pave the way to understand the classical spin-liquid behavior in many singlet ground state systems based on transition metal, rare-earth, and actinide compounds.

The muon and neutron data are available from the authors upon request.

ACKNOWLEDGMENTS

D.T.A. would like to thank the Royal Society of London for the Newton Advanced Fellowship funding between the United Kingdom and China and International Exchange funding between the United Kingdom and Japan. D.T.A. also thanks EPSRC UK for funding (Grant No. EP/W00562X/1). J.S. would like to thank the European Union's Horizon 2020 research and innovation program under Marie Skłodowska-Curie Grant Agreement No. 665593 awarded to the Science and Technology Facilities Council. E.V.S. thanks the Department of Atomic Energy, Government of India, for awarding the Raja Ramanna Fellowship (Order No. 1003/4/2021/RRF/R&D-II/8335). We thank the ISIS facility for providing the beam time.

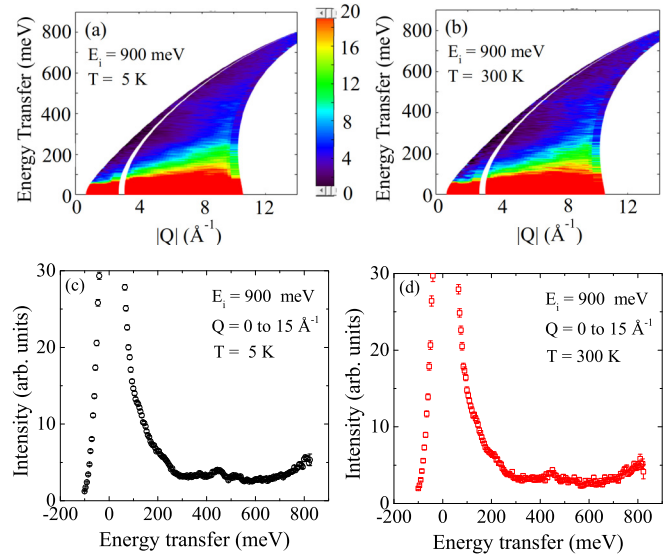

FIG. 10. Color-coded INS intensity map of the energy E transfer vs momentum $|Q|$ transfer for Sr_3NiPtO_6 measured at (a) 5 K and (b) 300 K with neutrons of incident energy $E_i = 900$ meV. $|Q|$-integrated (between 0 and 15 $Å^{-1}$) one-dimensional energy cuts of INS responses at (c) 5 K and (d) 300 K.

APPENDIX: INS DATA MEASURED WITH $E_i = 900$ meV

Figure 10 shows color-coded intensity maps of E transfer vs $|Q|$ transfer for Sr_3NiPtO_6 measured at 5 and 300 K with $E_i = 900$ meV along with plots of Q-integrated one-dimensional energy cuts.

[1] T. N. Nguyen and H.-C. zur Loye, A family of one-dimensional oxides: Sr_3MlrO_6 (M = Ni, Cu, Zn): Structure and magnetic properties, J. Solid State Chem. **117**, 300 (1995).

[2] T. N. Nguyen, D. M. Giaquinta, and H.-C. zur Loye, Synthesis of the new one-dimensional compound Sr_3NiPtO_6: Structure and magnetic properties, Chem. Mater. **6**, 1642 (1994).

[3] J. B. Claridge, R. C. Layland, W. H. Henley, and H.-C. zur Loye, Crystal growth and magnetic measurements on aligned single crystals of the oxides Sr_3NiPtO_6 and Sr_3CuPtO_6, Chem. Mater. **11**, 1376 (1999).

[4] G. V. Vajenine, R. Hoffmann, and H.-C. zur Loye, The electronic structures and magnetic properties of one-dimensional ABO_6 chains in Sr_3ABO_6 (A = Co, Ni; B = Pt, Ir) and two-dimensional MO_3 sheets in $InMO_3$ (M = Fe, Mn), Chem. Phys. **204**, 469 (1996).

[5] S. Niitaka, H. Kageyama, M. Kato, K. Yoshimura, and K. Kosuge, Synthesis, crystal structure, and magnetic properties of new one-dimensional oxides Ca_3CoRhO_6 and Ca_3FeRhO_6, J. Solid State Chem. **146**, 137 (1999).

[6] E. V. Sampathkumaran, N. Fujiwara, S. Rayaprol, P. K. Madhu, and Y. Uwatoko, Magnetic behavior of Co ions in the exotic spin-chain compound $Ca_3Co_2O_6$ from ^{59}Co NMR studies, Phys. Rev. B **70**, 014437 (2004).

[7] K. Takubo, T. Mizokawa, S. Hirata, J.-Y. Son, A. Fujimori, D. Topwal, D. D. Sarma, S. Rayaprol, and E.-V. Sampathkumaran, Electronic structure of Ca_3CoXO_6 (X = Co, Rh, Ir) studied by x-ray photoemission spectroscopy, Phys. Rev. B **71**, 073406 (2005).

[8] S. Agrestini, C. L. Fleck, L. C. Chapon, C. Mazzoli, A. Bombardi, M. R. Lees, and O. A. Petrenko, Slow magnetic order-order transition in the spin chain antiferromagnet $Ca_3Co_2O_6$, Phys. Rev. Lett. **106**, 197204 (2011).

[9] E. V. Sampathkumaran and A. Niazi, Superparamagnetic-like ac susceptibility behavior in the partially disordered antiferromagnetic compound Ca_3CoRhO_6, Phys. Rev. B **65**, 180401(R) (2002).

[10] E. V. Sampathkumaran, Z. Hiroi, S. Rayaprol, and Y. Uwatoko, Heat-capacity anomalies in the presence of high magnetic fields in the spin-chain compound, $Ca_3Co_2O_6$, J. Magn. Magn. Mater. **284**, L7 (2004).

[11] E. V. Sampathkumaran, N. Mohapatra, S. Rayaprol, and K. K. Iyer, Magnetic anomalies in the spin-chain compound Sr_3CuRhO_6: Griffiths-phase-like behavior of magnetic susceptibility, Phys. Rev. B **75**, 052412 (2007).

[12] S. Takeshita, J. Arai, T. Goko, K. Nishiyama, and K. Nagamine, Muon spin relaxation study of partially disordered state in

triangular-lattice antiferromagnet: $Ca_3Co_2O_6$, J. Phys. Soc. Jpn. **75**, 034712 (2006).

[13] S. Niitaka, K. Yoshimura, K. Kosuge, M. Nishi, and K. Kakurai, Partially disordered antiferromagnetic phase in Ca_3CoRhO_6, Phys. Rev. Lett. **87**, 177202 (2001).

[14] T. Basu, K. Iyer, K. Singh, K. Mukherjee, P. Paulose, and E. Sampathkumaran, Anisotropic magnetodielectric coupling behavior of $Ca_3Co_{1.4}Rh_{0.6}O_6$ due to geometrically frustrated magnetism, Appl. Phys. Lett. **105**, 102912 (2014).

[15] P. Núñez, S. Trail, and H.-C. zur Loye, Synthesis, crystal structure, and magnetic properties of Sr_3MgMO_6 (M = Pt, Ir, Rh), J. Solid State Chem. **130**, 35 (1997).

[16] C. Lampe-Önnerud, M. Sigrist, and H.-C. zur Loye, Crystal structure and magnetic properties of the one-dimensional oxide, Sr_3ZnIrO_6: Zinc in trigonal prismatic coordination, J. Solid State Chem. **127**, 25 (1996).

[17] R. C. Layland and H.-C. zur Loye, Synthesis, characterization, and magnetic properties of a commensurate and incommensurate phase of Sr_3ZnRhO_6: Zinc in trigonal prismatic coordination, J. Alloys Compd. **299**, 118 (2000).

[18] A. D. Hillier, D. T. Adroja, W. Kockelmann, L. C. Chapon, S. Rayaprol, P. Manuel, H. Michor, and E. V. Sampathkumaran, Noncollinear magnetic order in the $S = 1/2$ magnet Sr_3ZnRhO_6, Phys. Rev. B **83**, 024414 (2011).

[19] A. Niazi, E. V. Sampathkumaran, P. L. Paulose, D. Eckert, A. Handstein, and K. H. Müller, Sr_3CuIrO_6, a spin-chain compound with random ferromagnetic-antiferromagnetic interactions, Solid State Commun. **120**, 11 (2001).

[20] A. Niazi, E. V. Sampathkumaran, P. L. Paulose, D. Eckert, A. Handstein, and K. H. Müller, Magnetic anomalies in the spin-chain system $Sr_3Cu_{1-x}Zn_xIrO_6$, Phys. Rev. B **65**, 064418 (2002).

[21] W.-G. Yin, X. Liu, A. M. Tsvelik, M. P. M. Dean, M. H. Upton, J. Kim, D. Casa, A. Said, T. Gog, T. F. Qi, G. Cao, and J. P. Hill, Ferromagnetic exchange anisotropy from antiferromagnetic superexchange in the mixed 3*d*-5*d* transition-metal compound Sr_3CuIrO_6, Phys. Rev. Lett. **111**, 057202 (2013).

[22] X. Liu, V. M. Katukuri, L. Hozoi, W.-G. Yin, M. P. M. Dean, M. H. Upton, J. Kim, D. Casa, A. Said, T. Gog, T. F. Qi, G. Cao, A. M. Tsvelik, J. van den Brink, and J. P. Hill, Testing the validity of the strong spin-orbit-coupling limit for octahedrally coordinated iridate compounds in a model system Sr_3CuIrO_6, Phys. Rev. Lett. **109**, 157401 (2012).

[23] P. A. McClarty, A. D. Hillier, D. T. Adroja, D. D. Khalyavin, S. Rayaprol, P. Manuel, W. Kockelmann, and E. V. Sampathkumaran, Non-collinear order and spin-orbit coupling in Sr_3ZnIrO_6, J. Phys. Soc. Jpn. **89**, 064703 (2020).

[24] S. Toth, W. Wu, D. T. Adroja, S. Rayaprol, and E. V. Sampathkumaran, Frustrated Ising chains on the triangular lattice in Sr_3NiIrO_6, Phys. Rev. B **93**, 174422 (2016).

[25] D. Flahaut, S. Hébert, A. Maignan, V. Hardy, C. Martin, M. Hervieu, M. Costes, B. Raquet, and J. M. Broto, A magnetic study of the one dimensional Sr_3NiIrO_6 compound, Eur. Phys. J. B **35**, 317 (2003).

[26] G. R. Zhang, X. L. Zhang, T. Jia, Z. Zeng, and H. Q. Lin, Intrachain antiferromagnetic interaction and Mott state induced by spin-orbit coupling in Sr_3NiIrO_6, J. Appl. Phys. **107**, 09E120 (2010).

[27] D. Mikhailova, B. Schwarz, A. Senyshyn, A. M. T. Bell, Y. Skourski, H. Ehrenberg, A. A. Tsirlin, S. Agrestini, M. Rotter, P. Reichel, J. M. Chen, Z. Hu, Z. M. Li, Z. F. Li, and L. H. Tjeng, Magnetic properties and crystal structure of Sr_3CoIrO_6 and Sr_3NiIrO_6, Phys. Rev. B **86**, 134409 (2012).

[28] X. Ou and H. Wu, Impact of spin-orbit coupling on the magnetism of Sr_3MIrO_6 (M = Ni, Co), Sci. Rep. **4**, 4609 (2014).

[29] E. Lefrancois, L. C. Chapon, V. Simonet, P. Lejay, D. Khalyavin, S. Rayaprol, E. V. Sampathkumaran, R. Ballou, and D. T. Adroja, Magnetic order in the frustrated Ising-like chain compound Sr_3NiIrO_6, Phys. Rev. B **90**, 014408 (2014).

[30] T. Birol, K. Haule, and D. Vanderbilt, Nature of the magnetic interactions in Sr_3NiIrO_6, Phys. Rev. B **98**, 134432 (2018).

[31] K. R. Ó Neal, A. Paul, A. Al-Wahish, K. D. Hughey, A. L. Blockmon, X. Luo, S.-W. Cheong, V. S. Zapf, C. V. Topping, J. Singleton, M. Ozerov, T. Birol, and J. L. Musfeldt, Spin-lattice and electron-phonon coupling in 3d/5d hybrid Sr_3NiIrO_6, npj Quantum Mater. **4**, 48 (2019).

[32] N. Mohapatra, K. K. Iyer, S. Rayaprol, and E. V. Sampathkumaran, Geometrically frustrated magnetic behavior of Sr_3NiRhO_6 and Sr_3NiPtO_6, Phys. Rev. B **75**, 214422 (2007).

[33] S. Sarkar, S. Kanungo, and T. Saha-Dasgupta, *Ab initio* study of low dimensional quantum spin systems Sr_3NiPtO_6, Sr_3CuPtO_6, and Sr_3NiIrO_6, Phys. Rev. B **82**, 235122 (2010).

[34] S. Chattopadhyay, D. Jain, V. Ganesan, S. Giri, and S. Majumdar, Observation of large-D magnetic phase in Sr_3NiPtO_6, Phys. Rev. B **82**, 094431 (2010).

[35] S. K. Pandey and K. Maiti, Study of magnetic interactions in a geometrically frustrated compound, Sr_3NiPtO_6, using density functional approach, Europhys. Lett. **88**, 27002 (2009).

[36] A.-M. Pradipto, R. Broer, and S. Picozzi, Ab initio modelling of magnetic anisotropy in Sr_3NiPtO_6, Phys. Chem. Chem. Phys. **18**, 4078 (2016).

[37] S. N. Jammalamadaka, N. Mohapatra, K. K. Iyer, and E. V. Sampathkumaran, Insensitivity of magnetic anomalies in Sr_3NiPtO_6 to positive and negative pressures, J. Alloys Compd. **484**, 50 (2009).

[38] H. Tasaki, Quantum liquid in antiferromagnetic chains: A stochastic geometric approach to the Haldane gap, Phys. Rev. Lett. **66**, 798 (1991).

[39] W. Chen, K. Hida, and B. C. Sanctuary, Ground-state phase diagram of $S = 1$ XXZ chains with uniaxial single-ion-type anisotropy, Phys. Rev. B **67**, 104401 (2003).

[40] A. D. Hillier, P. J. C. King, S. P. Cottrell, and J. S. Lord, *The MuSR User Guide* (Rutherford Appleton Laboratory, Oxford, 2005).

[41] S. J. Blundell, Spin-polarized muons in condensed matter physics, Contemp. Phys. **40**, 175 (1999).

[42] A. D. Hillier, S. J. Blundell, I. McKenzie, I. Umegaki, L. Shu, J. A. Wright, T. Prokscha, F. Bert, K. Shimomura, A. Berlie, H. Alberto, and I. Watanabe, Muon spin spectroscopy, Nat. Rev. Methods Primers **2**, 4 (2022)

[43] V. K. Anand and D. C. Johnston, Antiferromagnetism in $EuCu_2As_2$ and $EuCu_{1.82}Sb_2$ single crystals, Phys. Rev. B **91**, 184403 (2015).

[44] V. K. Anand, D. A. Tennant, and B. Lake, Investigations of the effect of nonmagnetic Ca substitution for magnetic Dy on spin-freezing in $Dy_2Ti_2O_7$, J. Phys.: Condens. Matter **27**, 436001 (2015).

[45] Y. J. Uemura, A. Keren, K. Kojima, L. P. Le, G. M. Luke, W. D. Wu, Y. Ajiro, T. Asano, Y. Kuriyama, M. Mekata, H. Kikuchi, and K. Kakurai, Spin fluctuations in frustrated kagomé lattice system $SrCr_8Ga_4O_{19}$ studied by muon spin relaxation, Phys. Rev. Lett. **73**, 3306 (1994).

[46] R. Sarkar, Ph. Schlender, V. Grinenko, E. Haeussler, P. J. Baker, Th. Doert, and H.-H. Klauss, Quantum spin liquid ground state in the disorder free triangular lattice $NaYbS_2$, Phys. Rev. B **100**, 241116(R) (2019).

[47] Y. Li, D. Adroja, P. K. Biswas, P. J. Baker, Q. Zhang, J. Liu, A. A. Tsirlin, P. Gegenwart, and Q. Zhang, Muon spin relaxation evidence for the U(1) quantum spin-liquid ground state in the triangular antiferromagnet $YbMgGaO_4$, Phys. Rev. Lett. **117**, 097201 (2016).

[48] P. J. Brown, Magnetic form factors, in *International Tables for Crystallography*, Vol. C, *Mathematical, Physical and Chemical Tables*, edited by A. J. C. Wilson (Kluwer Academic, Amsterdam, 1999), pp. 450–457.

[49] M. Rotter, M. D. Le, A. T. Boothroyd, and J. A. Blanco, Dynamical matrix diagonalization for the calculation of dispersive excitations, J. Phys.: Condens. Matter **24**, 213201 (2012).

[50] K. W. H. Stevens, Matrix elements and operator equivalents connected with the magnetic properties of rare earth ions, Proc. Phys. Soc. A **65**, 209 (1952).

[51] A. Abragam and B. Bleaney, *Electron Paramagnetic Resonance of Transition Ions*, Oxford Classic Texts in the Physical Sciences (Oxford University Press, Oxford, 1970), p. 872.

[52] G. T. Trammell, Magnetic ordering properties of rare-earth ions in strong cubic crystal fields, Phys. Rev. **131**, 932 (1963).

[53] B. R. Cooper, Magnetic properties of compounds with singlet ground state: Exchange correlation effects, Phys. Rev. **163**, 444 (1967).

[54] Y. L. Wang and B. R. Cooper, Collective excitations and magnetic ordering in materials with singlet crystal-field ground state, Phys. Rev. **172**, 539 (1968).

[55] D. C. Johnston, Magnetic susceptibility of collinear and noncollinear Heisenberg antiferromagnets, Phys. Rev. Lett. **109**, 077201 (2012).

[56] D. C. Johnston, Unified molecular field theory for collinear and noncollinear Heisenberg antiferromagnets, Phys. Rev. B **91**, 064427 (2015).

[57] J. G. Rau and M. J. P. Gingras, Frustrated quantum rare-earth pyrochlores, Annu. Rev. Condens. Matter Phys. **10**, 357 (2019).

[58] C. Broholm, R. J. Cava, S. A. Kivelson, D. G. Nocera, M. R. Norman, and T. Senthil, Quantum spin liquids, Science **367**, eaay0668 (2020).

[59] P. W. Anderson, Resonating valence bonds: A new kind of insulator? Mater. Res. Bull. **8**, 153 (1973).